The Evolution and Propagation of Quasigeostrophic Ocean Eddies*

JEFFREY J. EARLY, R. M. SAMELSON, AND DUDLEY B. CHELTON

College of Oceanic and Atmospheric Sciences, Oregon State University, Corvallis, Oregon

(Manuscript received 13 October 2010, in final form 25 February 2011)

ABSTRACT

The long-term evolution of initially Gaussian eddies is studied in a reduced-gravity shallow-water model using both linear and nonlinear quasigeostrophic theory in an attempt to understand westward-propagating mesoscale eddies observed and tracked by satellite altimetry. By examining both isolated eddies and a large basin seeded with eddies with statistical characteristics consistent with those of observed eddies, it is shown that long-term eddy coherence and the zonal wavenumber–frequency power spectral density are best matched by the nonlinear model. Individual characteristics of the eddies including amplitude decay, horizontal length scale decay, and zonal and meridional propagation speed of a previously unrecognized quasistable state are examined. The results show that the meridional deflections from purely westward flow (poleward for cyclones and equatorward for anticyclones) are consistent with satellite observations. Examination of the fluid transport properties of the eddies shows that an inner core of the eddy, defined by the zero relative vorticity contour, contains only fluid from the eddy origin, whereas a surrounding outer ring contains a mixture of ambient fluid from throughout the eddy's lifetime.

1. Introduction

Baroclinic Rossby waves have long been known to play an important role in the spinup of the ocean (Anderson and Gill 1975), and so their apparent direct observation through satellite altimetry measurements of global sea surface height (SSH) (Chelton and Schlax 1996) was a well celebrated result. These early observations were shown to differ in their predicted phase speed from linearized quasigeostrophic theory, which motivated numerous attempts to modify the classical theory (e.g., Killworth et al. 1997; Tailleux and McWilliams 2001; Killworth and Blundell 2005). However, subsequent observations from higher-resolution SSH fields constructed from multiple satellite altimeters have cast doubt on the original interpretation of the observations as linear waves (Chelton et al. 2007, 2011). The enhanced observations now show more eddy-like structures that remain coherent for long durations, with opposing meridional deflections for cyclones and anticyclones, and suggest a significant degree of nonlinearity through several nondimensional parameters. Motivated by these observations, we examine the basic characteristics of Rossby waves and eddies in a standard quasigeostrophic setting.

We consider both linear ($\beta^{-1} = 0$) and nonlinear ($\beta^{-1} \neq 0$) quasigeostrophic theory in a reduced-gravity shallow-water model,

$$\frac{\partial}{\partial t}(\nabla^2\eta - \eta) + \frac{\partial \eta}{\partial x} + \beta^{-1} \cdot J(\eta, \nabla^2\eta) = 0, \qquad (1)$$

where the dimensionless variable $\eta(x, y, t)$ is a sea level height perturbation scaled by a representative value η_0 and the Jacobian is defined as $J(a, b) = a_x b_y - a_y b_x$. The nondimensional coefficient $\beta^{-1} = U/(\beta_0 L_R^2)$, where $U = g\eta_0/(f_0 L_R)$ is the geostrophic velocity scale associated with η_0, g is the acceleration of gravity, β_0 is the meridional gradient of the Coriolis parameter, and L_R is the Rossby radius of deformation. Equation (1) is typically written with the nondimensional parameter β associated with the planetary vorticity term $[\beta(\partial\eta/\partial x)]$; however, the convention used here uses the long-wave time scale of $(\beta_0 L_R)^{-1}$ rather than the advective time scale L_R/U so that Eq. (1) reduces to a parameter independent form of the linearized Rossby wave equation when $\beta^{-1} = 0$.

* Supplemental information related to this paper is available at the Journals Online Web site: http://dx.doi.org/10.1175/2011JPO4601.s1.

Corresponding author address: Jeffrey J. Early, College of Oceanic and Atmospheric Sciences, 104 COAS Admin. Bldg., Oregon State University, Corvallis, OR 97331.
E-mail: jeffrey@jeffreyearly.com

DOI: 10.1175/2011JPO4601.1

In the first set of experiments presented here, the linear ($\beta^{-1} = 0$) and nonlinear evolution of individual Gaussian initialized eddies (Ae^{-r^2/L^2}, where A is the amplitude and L is the radial length scale) are first compared, and it is shown that the long-term coherence of the observed eddies cannot be explained by the linear theory. For the linear and nonlinear cases, a basin is then seeded continuously for 150 yr with Gaussian eddies with statistical characteristics that approximate those of the eddies observed with altimetry. By considering the zonal wavenumber–frequency power spectral density, we are able to compare model results with observations and it is shown that linear theory does not explain the observed spectra and must be rejected.

In the second set of experiments, isolated Gaussian initial conditions are modeled with the nonlinear equation for time durations much longer than in past studies. It is shown that a previously unrecognized quasi-stable eddy state emerges. Individual characteristics of these eddies are then diagnosed including amplitude decay, horizontal length scale decay, propagation speed, and fluid transport properties. These provide baseline properties for comparison with the observations and other theories. It is shown that the meridional deflections from due westward propagation, the transport properties, and zonal propagation speeds are generally consistent with those of observed eddies.

2. Nonlinear dynamics

a. Waves versus eddies

To compare wave-like and eddy-like mesoscale features, consider the single Rossby plane wave solution to the fully nonlinear quasigeostrophic Eq. (1),

$$\eta(x, y, t) = N_0 \cos(kx + ly - \omega t + \phi), \qquad (2)$$

where N_0 is a constant amplitude, k and l are zonal and meridional wavenumbers, $\omega = -k/(k^2 + l^2 + 1)$ is the nondimensional frequency, and ϕ is a constant phase (Pedlosky 1987). Although Eq. (2) solves both the linearized and nonlinear form of Eq. (1), only for $\beta^{-1} = 0$ do linear combinations of Rossby waves solve the nonlinear Eq. (1). For long wavelengths, k, $l \ll 1$, the linearized form of the equation is only weakly dispersive and so it is conceivable that linear features might remain coherent for long durations as observed in the altimetry data.

An initial comparison between the linear and nonlinear form of the equation can be made by considering the evolution of an initially Gaussian sea surface height perturbation. For all model runs, an equivalent depth of $D = 80$ cm (gravity wave phase speed of 2.8 m s^{-1}) was used at latitude 24°. This could equivalently be thought of as a single 800-m layer with reduced gravitational acceleration of approximately 1 cm s^{-2}. This corresponds to the observed deformation radius $L_R = 47$ km along 24° in the eastern North Pacific (Chelton et al. 1998) with time scale $(\beta_0 L_R)^{-1}$ of 12 days, and the long-wave Rossby wave speed is therefore $c_x = \beta_0 L_R^2 = 4.7$ cm s^{-1}. For a scale height of 10 cm these parameters require setting $\beta^{-1} = 7.5$, whereas for the linear form of the equation they require setting $\beta^{-1} = 0$.

An initial perturbation of $\eta(x, y, 0) = N_0 e^{-r^2/L^2}$ with amplitude $N_0 = 15$ cm and length scale $L = 80$ km was modeled for 365 days using the two forms of the equation; the results are shown in Fig. 1. The linear evolution is dominated by Rossby wave interference patterns, although the sea surface maximum can still be observed to propagate westward. The nonlinear evolution also shows Rossby wave interference patterns but is dominated by the coherent westward-propagating sea surface maximum. The nonlinear anticyclonic eddy also shows a much slower amplitude decay rate and an equatorward deflection (McWilliams and Flierl 1979), both qualitatively consistent with the observations reported by Morrow et al. (2004) and Chelton et al. (2007, 2011).

All experiments used pseudospectral methods (Canuto 2006) to compute spatial derivatives and fourth-order Runge–Kutta time stepping to iterate forward in time, still one of the more accurate and efficient iterative techniques available (Durran 1991). To ensure numerical stability, spectral vanishing viscosity was used to prevent the buildup of energy at higher wavenumbers (Tadmor 1989). The premise is to construct a typical low-order hyperviscosity operator, like those found in McWilliams and Flierl (1979) or Maltrud and Vallis (1993), but then to filter this operator such that low wavenumbers are completely undamped. The original results obtained in Tadmor (1989) that restrict the choices of this filter are nicely reviewed in Karamanos and Karniadakis (2000). This approach has since been used in other fluid models with great success (Gelb and Gleeson 2001; Pasquetti 2005). Because the domain is doubly periodic, a sponge layer was added to all four sides to prevent signals from crossing the boundaries. The numerical model was validated by comparison with the steady dipole solution found analytically in Flierl et al. (1980), by doubling the resolution of all experiments from 4 to 2 km, and by varying the damping techniques and damping parameters.

b. Eddy seeding experiment

To compare the wavenumber–frequency spectra of observations with those of the linear and nonlinear models, a basin 8300 km × 3850 km was seeded by modifying the instantaneous streamfunction at a random sequence of times during the full 150 yr of the simulation

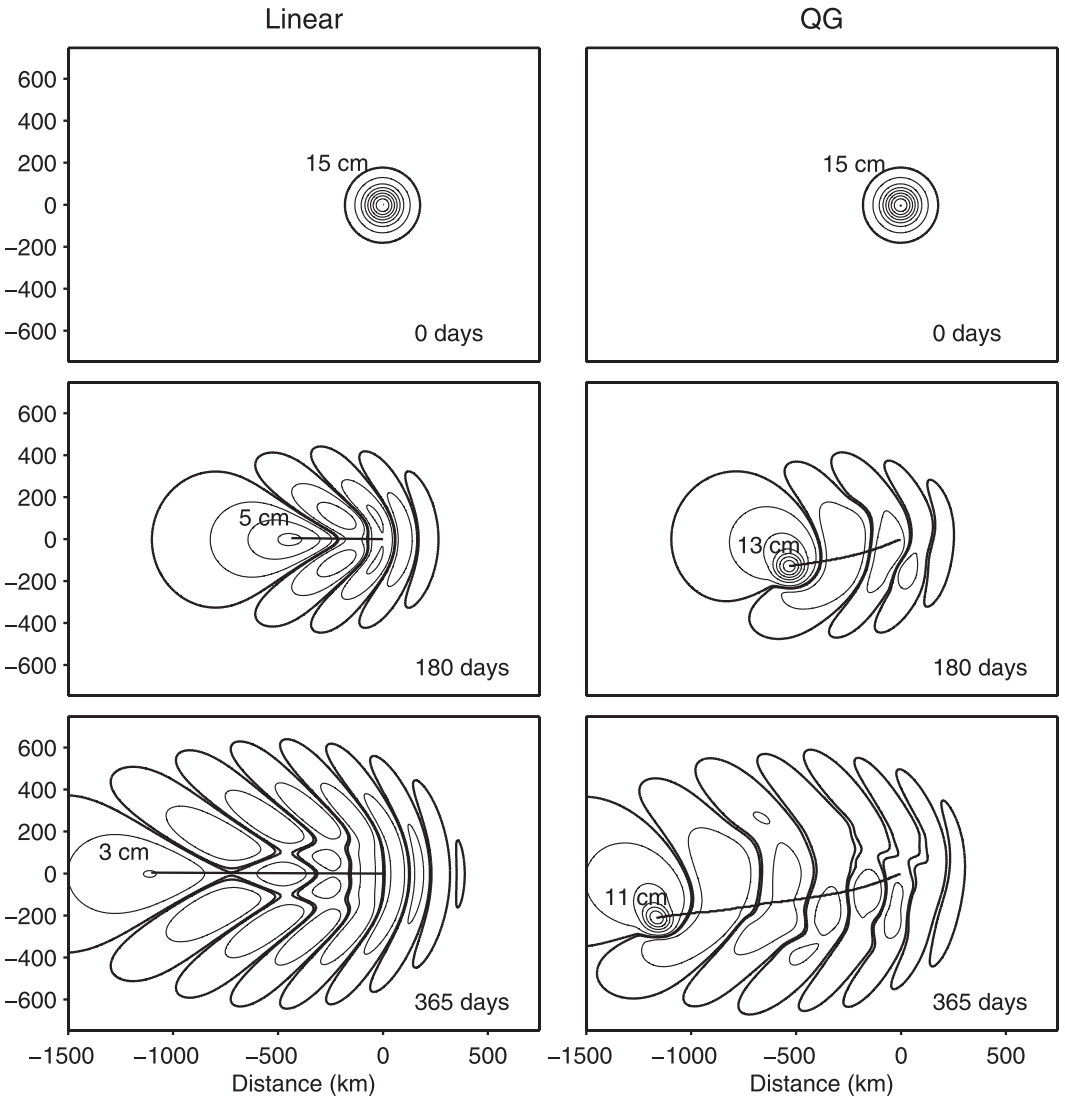

FIG. 1. The evolution of an initially Gaussian SSH of amplitude 15 cm and length scale 80 km. The linear form of Eq. (1) with (left) $\beta^{-1} = 0$ and (right) the value appropriate for the first baroclinic mode at 24° latitude, $\beta^{-1} = 7.5$. The contours are drawn for every 2 cm of height at odd values (e.g., −1, 1, 3 cm, etc.), and a thicker contour is drawn at 0 cm to emphasize the interference pattern. The thick black line is the path of the SSH maximum. Animations for the two cases shown in this figure are available in the supplemental material at the Journals Online Web site: http://dx.doi.org/10.1175/2011JPO4601.s1.

with Gaussian eddies placed at random locations throughout the domain. The seeded eddies had amplitudes (both positive and negative), horizontal length scale distributions, and spatial and temporal frequencies of occurrence that matched the statistics of the observed eddies in a region of the subtropical North Pacific (Chelton et al. 2011). The simulation was run and continuously seeded with these eddies throughout the domain for 150 yr.

The sea surface height 13 yr into the two model runs is shown in Fig. 2. Because the linear model simply evolves the phases of individual Rossby waves, the energy at individual wavenumbers cannot transfer to other wavenumbers and changes only by virtue of the energy continuously added by the eddy seeds. The sea surface height for the linear model therefore consists of an evolving interference pattern from the superposition of waves with length scales unmodified from the original eddy seeds. Conversely, the nonlinear model allows interactions between wavenumbers and transfers energy to different scales just as in the study of quasigeostrophic turbulence (Vallis 2006). The nonlinear model run shows a clear trend toward reduced energy at short wavelengths (see Figs. 2, 3). Further, the eddies can be observed from the animations in the online supplemental material

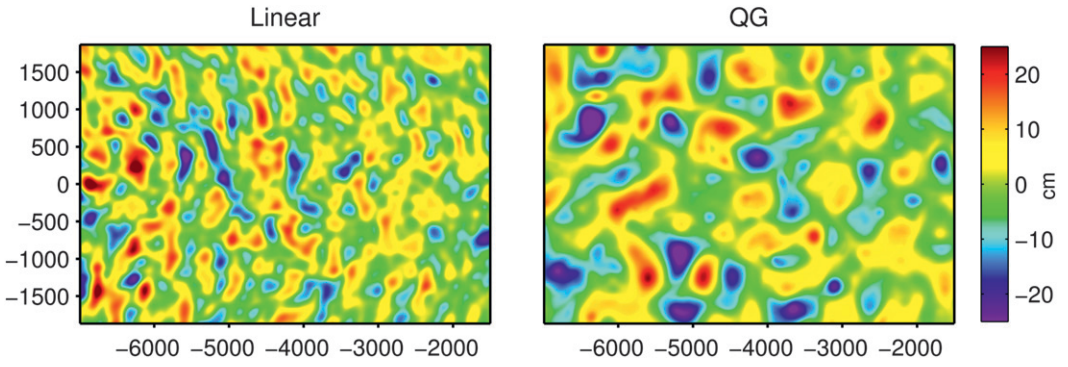

FIG. 2. SSH 13 yr into the eddy seeding experiment. Shown are (left) the evolved state using the linear equation and (right) the evolved state using the nonlinear equation. Both experiments were seeded with the exact same Gaussian eddies at the same times and locations. The domain shown is a subset of the entire modeled domain.

(available at the Journals Online Web site: http://dx.doi.org/10.1175/2011JPO4601.s1) to interact by distortions, changes in their propagation paths, and merging, unlike the linear case.

The zonal frequency–wavenumber spectra in Fig. 3 show very different behaviors between the two models. For the spatial domain, analysis was restricted to 1500 km west of the easternmost eddy seeds to a box 5500 km in zonal extent and 3600 km in meridional extent. For the linear model, the spectral power is restricted to frequencies below the meridional wavenumber $l = 0$ of the zonal Rossby wave dispersion relation. This is consistent with theory, because waves with given zonal (k) and nonzero meridional wavenumbers ($l \neq 0$) have frequencies that remain below the frequency for $l = 0$. The spectral power for the nonlinear model is distributed substantially differently than for the linear model. The signals are essentially nondispersive for lower wavenumbers for both models, whereas the energy at higher wavenumbers remains centered near the same nondispersive slope for the nonlinear model but not the linear model. The zonal frequency–wavenumber spectrum of the nonlinear model is very similar to that of the observations in Fig. 4, whereas the linear model fails to explain the nondispersive structure observed.

It is noteworthy that small ''spurs'' of spectral power extend a short distance along the dispersion relation for both the model and the observations. In the case of the observations, it is not clear from Fig. 4 whether this spur of spectral variance is more consistent with either of the modified Rossby wave theories than with the classical theory. Distinguishing between these theories is not an objective of this study, because the model considered here is not capable of representing the processes of vertical

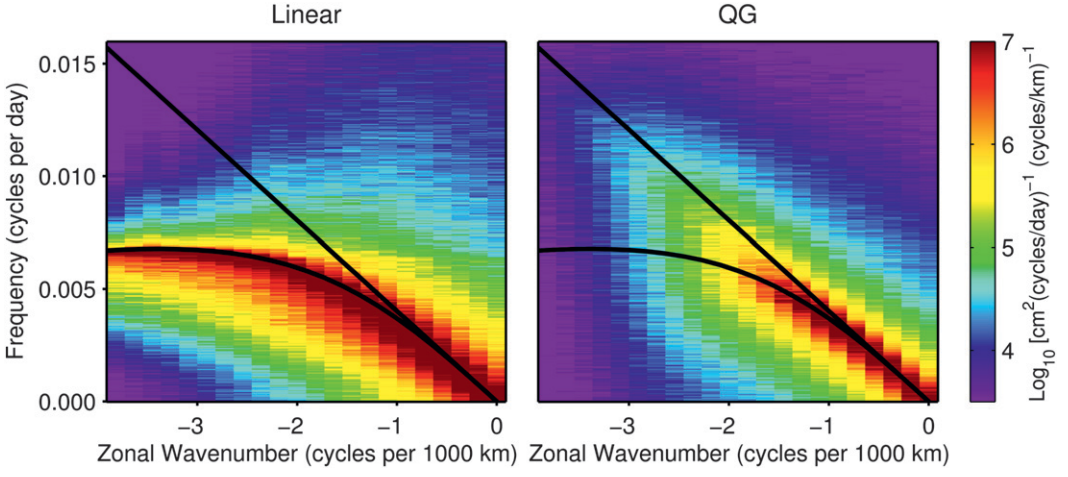

FIG. 3. Zonal frequency–wavenumber spectra for SSH of (left) the linear model and (right) the nonlinear model from 110 yr of the eddy seeding experiment; 25 neighboring latitude bands were ensemble averaged. The black lines are the maximum (meridional wavenumber $l = 0$) Rossby wave zonal dispersion relation (curved) and its nondispersive limit (linear).

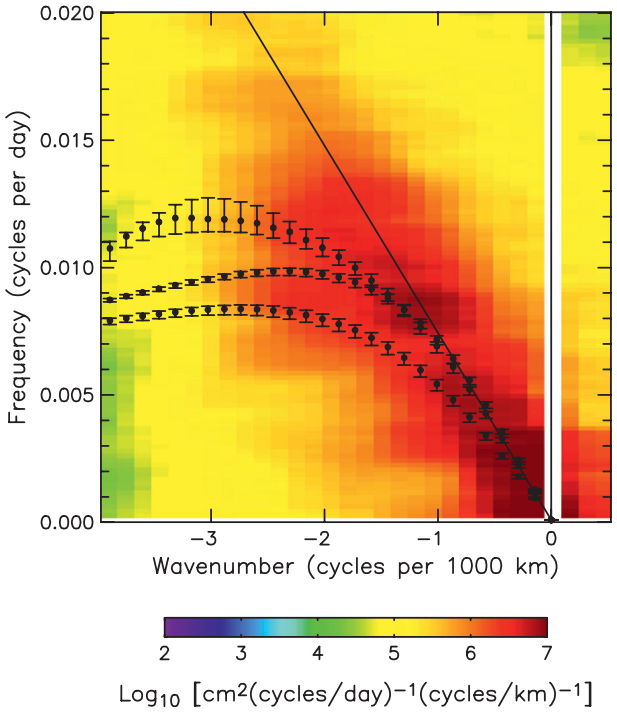

FIG. 4. Zonal frequency–wavenumber spectra for SSH from the merged Ocean Topography Experiment (TOPEX)/Poseidon–European Remote Sensing Satellite (ERS) satellite altimetry data along 24°N in the western subtropical Pacific Ocean. The solid line is computed from the radon transformation. The three dispersion relations shown are from standard Rossby wave theory, the rough bottom topography theory of Tailleux and McWilliams (2001), and the vertical shear-modified theory of Killworth et al. (1997) extended to the case of nonzero zonal wavenumber (Fu and Chelton 2001), in order of increasing frequency along the left-hand side of the plot.

shear or rough bottom topography that are the physical basis for the modified theories. The spur of spectral power along the dispersion relation in the case of the reduced-gravity model considered here is investigated in more detail from monopole experiments in section 4.

Figure 5 shows distributions of the deviation from due west propagation of the eddies in the eddy seeding experiments. The linear model shows no systematic preference for meridional deflection, matching the results of purely westward propagation found for the isolated Gaussian in Fig. 1. The spread of meridional deflection angles is evidently attributable to randomness in the interference patterns from the superposition of the waves in the linear solution. In contrast, the eddies tracked in the nonlinear model show distinct tendencies for poleward and equatorward deflection for cyclonic and anticyclonic eddies, respectively. This is consistent with the observations that show similarly opposing deflections of cyclones and anticyclones. However, in the observations, the mean deflection angle for combined cyclones and anticyclones is rotated a small but significant amount equatorward from due west (Chelton et al. 2011). This asymmetry about due west in the observations cannot be explained by quasigeostrophic theory because the meridional component of Eq. (1) is antisymmetric with a change in height polarity ($\eta \rightarrow -\eta$). The slight equatorward rotation of the mean deflection angle from due west in the observations may be an indication of the effects of meridional advection or the effects of vertical shear on the total potential vorticity gradient vector from ambient currents (Samelson 2010) that are not included in the zero mean flow, reduced-gravity model considered here.

Figure 6 shows the distributions of the tracked eddy speeds normalized by the long Rossby wave phase speed $c_x = \beta_0 L_R^2$. The mean value of the distribution for the linear model, $\mu = 0.54$, falls far below the mean value of the observations for the Northern Hemisphere, $\mu = 0.74$. However, the mean value of the distribution from nonlinear model, $\mu = 0.77$, shows a significant increase over the linear model that is comparable to the observations. The largest difference between the observations and the nonlinear model is in the variability of the distributions. The failure of the nonlinear model to capture the variability of the observations may be attributed to the simplicity of the nonlinear model, which includes only a single independent vertical mode and variations in the Coriolis parameter as the only contribution to the potential vorticity gradient; or, it could be an indication of the importance of nongeostrophic effects that are not included in the model.

The long-term coherence of the isolated eddies, the wavenumber–frequency spectra from the eddy seeding experiments, their meridional deflection, and their distribution of tracked speeds suggest that linearized quasigeostrophic theory is not a viable theory to explain the observed westward-propagating features. Nearly all of the observed properties are well explained by nonlinear quasigeostrophic theory confirming that the observed signal represents eddies obeying nonlinear dynamics rather than Rossby waves obeying linear dynamics.

3. Monopoles

a. The three states of evolution

The interest in eddies on a β plane has generated a long history of analytical and numerical models attempting to elucidate some of their basic properties, such as amplitude decay and propagation speeds and directions. The two-dimensional quasigeostrophic potential vorticity equation [Eq. (1)] lacks many of the complexities associated with multilayer quasigeostrophic or primitive equation models yet remains sufficiently complex that the

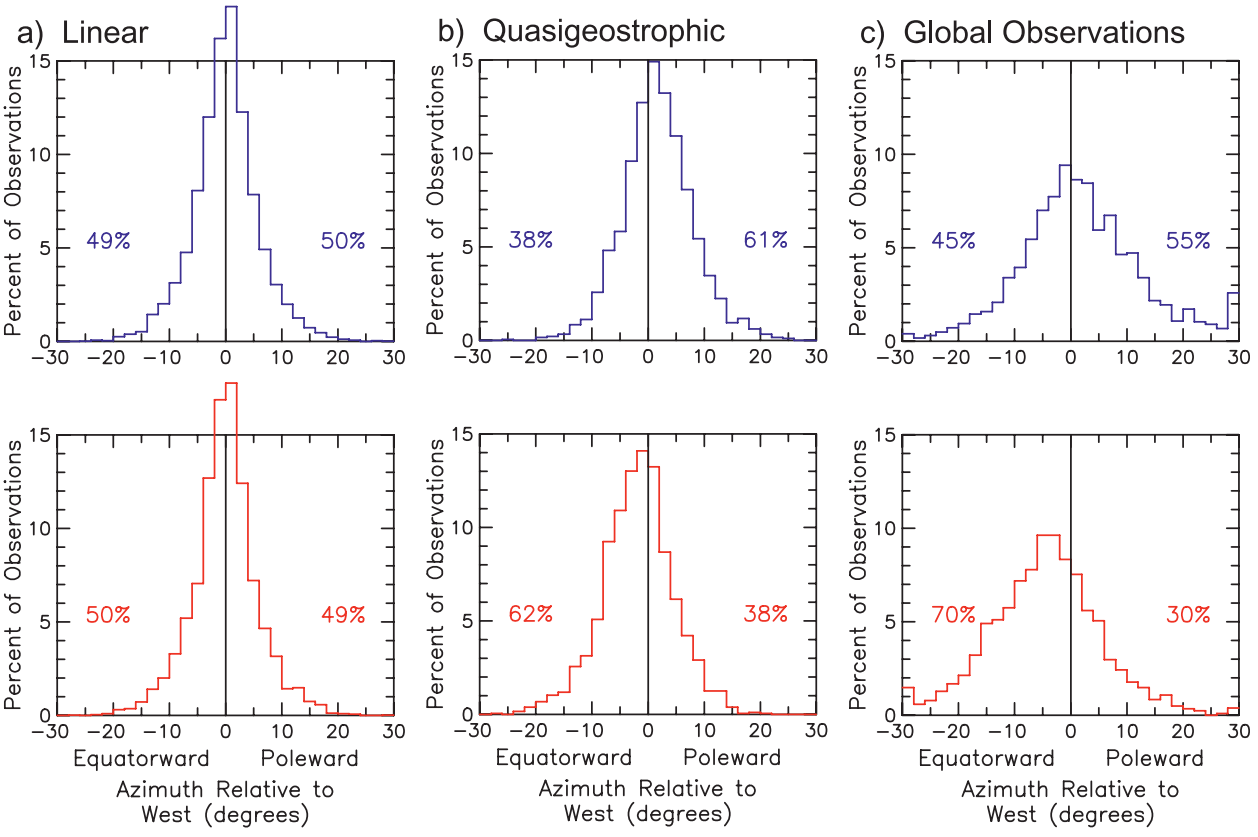

FIG. 5. Meridional deflection of the (top) cyclonic and (bottom) anticyclonic eddies. (a) The linear model shows no preference for equatorward or poleward deflection, whereas (b) the quasigeostrophic model shows cyclones have a poleward preference and anticyclones an equatorward preference. (c) The satellite observations show a pattern similar to quasigeostrophic dynamics, but with the mean propagation direction of the combined cyclonic and anticyclonic eddies rotated slightly equatorward.

evolution properties of Gaussian initialized disturbances are still not completely understood. Previous studies have typically recognized two distinct states in the evolution of a quasigeostrophic eddy: an initialization period followed by what was assumed to be a quasi-stable state (Sutyrin et al. 1994; Korotaev 1997; Reznik et al. 2000). Here, we will argue that there are actually three states: formation of the β gyre (initialization); an adjustment period (formerly believed to be quasi stable); and a third quasi-stable, slowly decaying state that has not previously been explored.

Typical amplitudes (5, 10, 15, and 20 cm) and radial length scales (40, 60, 80, 100, and 120 km) were used to initialize isolated Gaussians with parameters representative of latitude 24°N in the eastern North Pacific. These correspond to nondimensional amplitudes of 0.5, 1.0, 1.5, and 2.0 and nondimensional length scales of 0.85, 1.27, 1.69, 2.12, and 2.54. It is important to note that cyclonic eddies (negative amplitudes) can be safely omitted from consideration because Eq. (1) is symmetric when changing polarity, provided that the sign of y is flipped as well. Formally, if $s(x, y, t)$ is a solution to Eq. (1), then $\tilde{s}(x, y, t) = -s(x, -y, t)$ is also a solution of Eq. (1). Any conclusions drawn here for anticyclonic eddies therefore also apply to cyclonic eddies provided the terms equatorward and poleward are swapped.

For these Gaussian initializations, a quasi-stable westward-propagating eddy generally emerges as the dominant feature. When the model was initialized with non-Gaussian solitary shapes, other solutions were more likely to emerge (including eastward-propagating dipoles), but the quasi-stable westward-propagating eddy was still part of the solution, although sometimes with very different amplitude and length scale than the initialization shape. These quasi-stable eddies are the focus of this study, but we briefly consider the other two transient stages as well.

1) FORMATION OF THE β GYRE

The first component of an eddy's evolution is the formation of the β gyre, in which an initially axisymmetric eddy evolves an azimuthal mode-one component because of the β effect over a time scale $(\beta_0 L_R)^{-1} \approx$ 12 days (Fiorino and Elsberry 1989). The flow associated

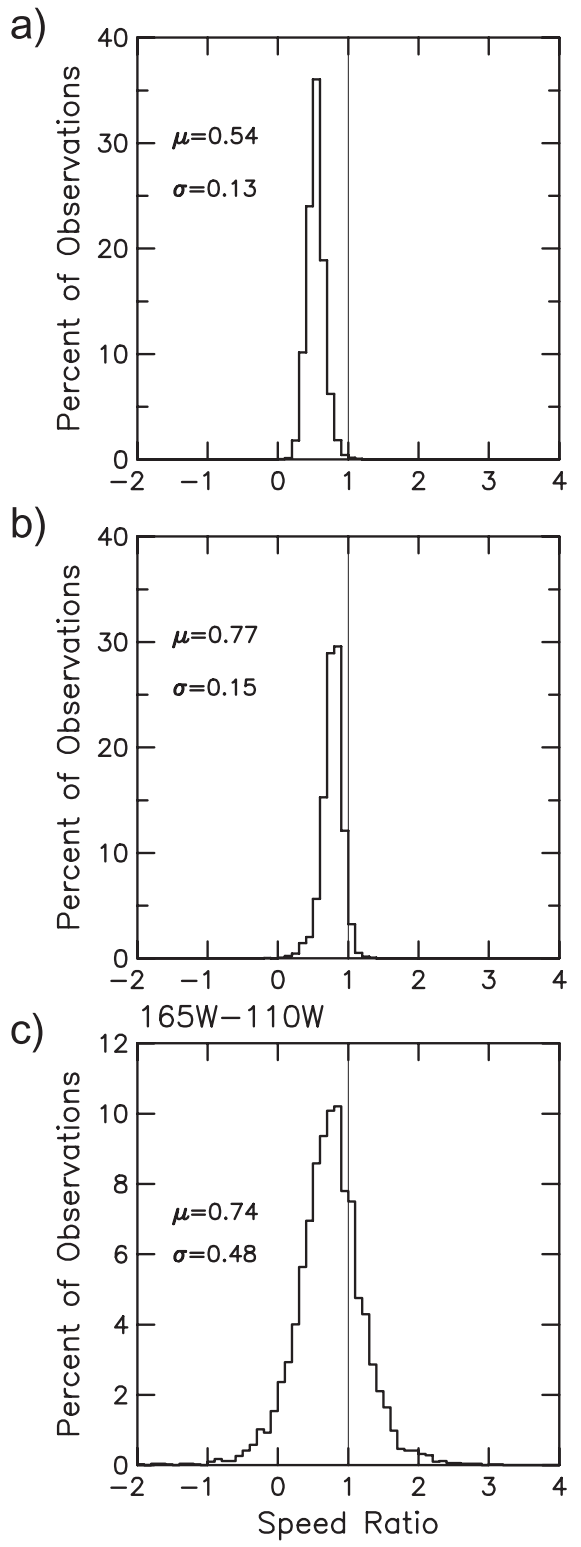

FIG. 6. Distributions of eddy speeds from the nonlinear model normalized by the nondispersive Rossby wave phase speed: (top)–(bottom) linear model, nonlinear model, altimeter observations. The altimeter observations include eddies in the eastern subtropical Pacific between 20° and 35°N and between 165° and 110°W.

with the dipole structure of the gyre initially causes a largely meridional deflection of the eddy, which then eventually propagates more zonally. Analytical predictions for the trajectory of an eddy have previously been found to agree well with numerical simulations for time periods less than $(\beta_0 L_R)^{-1}$, after which the radiation of Rossby waves strongly alters its evolution (Sutyrin and Flierl 1994; Reznik and Dewar 1994).

This initialization period must be expected because a Gaussian shape cannot be a stable solution for the quasigeostrophic potential vorticity equation [Eq. (1)]. A radially symmetric shape like a Gaussian causes the Jacobian to vanish, meaning that the advection of relative vorticity is trivial (advection is still present but moves fluid parcels to locations of fluid parcels with identical relative vorticity). Because the advective nonlinearity is initially trivial, linear Rossby wave dispersion due to the β effect will necessarily cause the initially Gaussian shape to become asymmetric as explored in Flierl (1977) (see Fig. 7). This asymmetry will in turn induce nontrivial advection of relative vorticity through the Jacobian term.

Here, we consider an explanation of the formation of the β gyre valid for this short time scale initialization period $t < (\beta_0 L_R)^{-1}$. The initial disturbance is a positive Gaussian and the resulting anticyclonic eddy can be thought of as either the local sea surface maximum or the local relative vorticity minimum. Recall that without the dispersive and advective terms in Eq. (1) the initial disturbance would propagate zonally with unaltered shape at exactly the linear long-wave speed. The evolution of the eddy can therefore be thought of as a deviation from perfectly zonal propagation by advection and dispersion.

(i) Because the initial disturbance is radially symmetric, the first time step is governed entirely by linear dynamics. The disturbance maximum moves westward; however, because of the dispersive relationship between the group velocity and wavelength, the signal associated with longer wavelengths will travel farther westward, whereas the signal associated with shorter wavelengths will travel more slowly westward (eastward for the very shortest wavelengths). The net effect is a decrease in the western slope and steepening of the eastern slope, evidently because the shorter wavelengths, which are required to describe steeper slopes, trail to the east of the longest wavelengths, which are required to describe shallower slopes.

(ii) As the gradient of the leading edge shallows and the gradient of the trailing edge steepens, advection plays a larger role (this is the formation of the β gyre). The

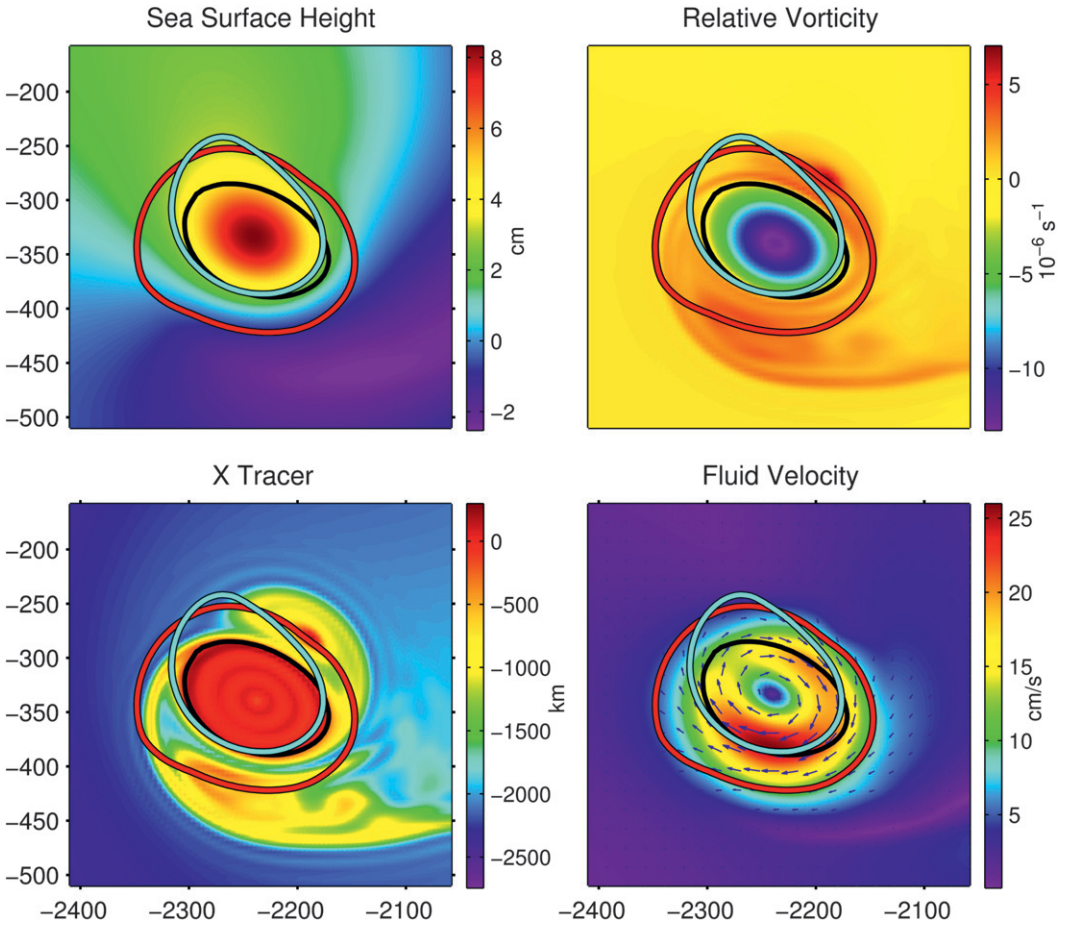

FIG. 7. Contours (color shading) of height, relative vorticity, zonal-coordinate tracer, and fluid velocity for a Gaussian initialized 15-cm-height, 80-km eddy on day 675 of its evolution. The *e*-fold contour (maximum height divided by *e*) is shown in cyan. The instantaneous closed height contour in the comoving frame (red) and the contour of zero relative vorticity (black) are also shown.

stronger equatorward flow on the east side of the anticyclonic eddy considered here and weaker poleward flow on the west side cause net equatorward meridional advection of fluid at the eddy's centroid and therefore an equatorward deflection of the anticyclonic eddy (McWilliams and Flierl 1979). Note that this requires a height difference across the eddy, consistent with the idea that the eddy formed from the initial disturbance is best described by relative vorticity contours rather than height contours, as elucidated in more detail later. The initially equatorward deflection is particularly strong because the net initial advection is exactly equatorward. The eddy therefore initially translates to the southwest for this Northern Hemisphere anticyclone.

(iii) After time periods of $t \sim (\beta_0 L_R)^{-1}$, an asymmetric shape of the eddy forms to provide a near advective–dispersive balance. This shape is characteristic of both the adjustment period that follows the β-gyre formation and the subsequent long-term quasi-stable state. Dispersion moves much of the signal to the region east of the eddy maximum (as can be seen in the linear case of Fig. 1), whereas advection moves fluid to the southwestern region. These two effects do not completely balance, with the difference being approximately an order of magnitude less than their respective individual values, and the net effect is to pull the eddy to the southeast from otherwise due westward propagation at the long-wave phase speed. Linear dispersion is responsible for slowing the westward propagation of the eddy, never quite reaching the linear 4.7 cm s^{-1} longwave speed (Flierl 1977), whereas the advection is responsible for deflecting the anticyclonic eddy equatorward (McWilliams and Flierl 1979).

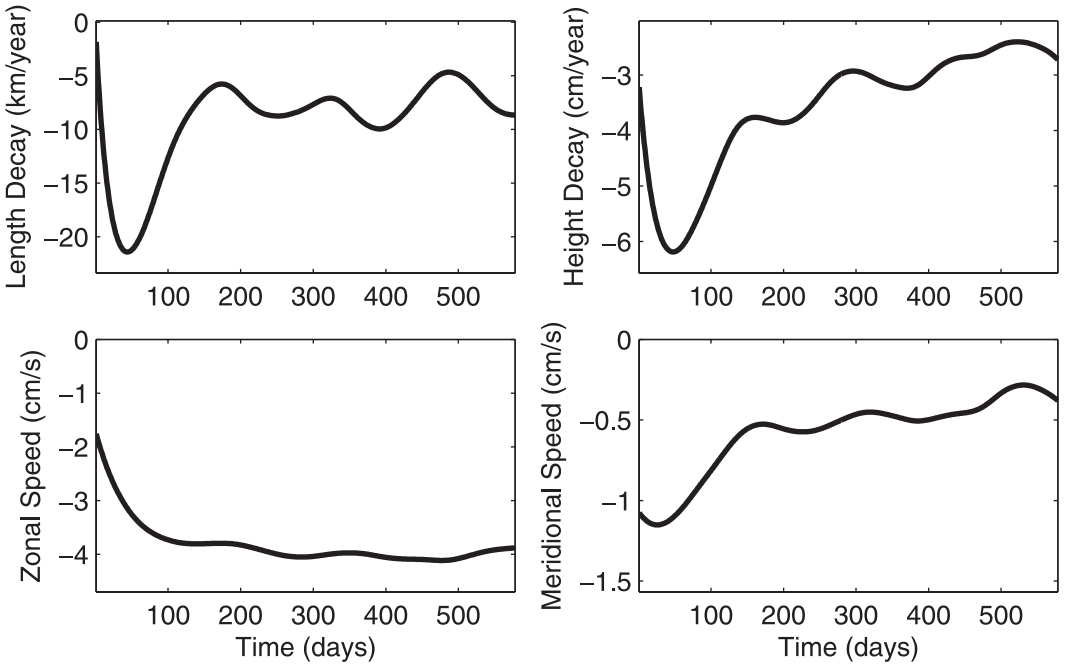

FIG. 8. Time evolution of four properties for a Gaussian eddy initialized with 15-cm-amplitude and 80-km-length scale: (top left) length scale decay rate, (top right) height decay rate, (bottom right) meridional speed, and (bottom left) zonal speed. The β-gyre formation (initialization) occurs for times less than 11 days and is therefore not well described in this figure. All four properties show the adjustment period of roughly 200 days before the eddy settles into the quasi-stable state. Note that the speed plots are shown with a different vertical axis and the meridional speed is nearly an order of magnitude slower than the zonal speed.

2) ADJUSTMENT PERIOD

After time periods of $t \sim (\beta_0 L_R)^{-1}$, the eddy's evolution is largely dictated by its energy loss due to the excitation of Rossby waves (Flierl 1984). Figure 8 shows changes in the decay rates of the length scale, amplitude, and the zonal and meridional speed over the first 600 days of the eddy evolution. There is a distinct adjustment period over the first 200 days, $t \sim 20(\beta_0 L_R)^{-1}$, where the changes are quite rapid. These values were obtained by tracking the relative vorticity extremum and recording the contour of zero relative vorticity, the local sea surface maximum, and the sea surface height *e*-fold contour.

It was noted in Sutyrin et al. (1994) that at around 175 days (converted to the scales used here) a tripole emerges in the potential vorticity field. The rapid changes in eddy properties during the end of the adjustment period (Fig. 8) may reflect processes associated with the emergence of this tripole structure. Perhaps not coincidentally, it is also around 200 days that analytical predictions of the eddy path show qualitatively poor agreement with numerical results (Sutyrin et al. 1994; Korotaev 1997; Reznik et al. 2000).

For most of the cases considered here, the transition from initialized Gaussian to quasi-stable, slowly decaying eddy followed the pattern shown in Fig. 8. However, some of the large length scale and small-amplitude Gaussians (which have smaller $U_{\max}$) took much longer and sometimes never even reached the quasi-stable state, instead dispersing with more wave-like characteristics due to the weak nonlinearity of these eddies. This is consistent with the results in Sutyrin et al. (1994), where it was found that, given their chosen length scale, there exists a critical intensity below which the tripole in the potential vorticity field failed to emerge. The length of the adjustment period depends on the height and length of the initial Gaussian, but for most cases the quasi-stable state is generally reached at approximately 100–200 days, $t \sim 15(\beta_0 L_R)^{-1}$.

3) QUASI-STABLE STATE

The quasi-stable eddy state for a Northern Hemisphere anticyclone always has the characteristic shape shown in Fig. 7 that is necessary for maintaining the near advective–dispersive balance. The height field is characterized by a steep south-southeastern edge, whereas the north-northwestern edge is particularly shallow. The resulting geostrophic velocity field consists of strong flow in the south-southeastern region and weak flow along the north-northwestern edge. The asymmetry in the height field is easily seen from the cyan *e*-fold contour.

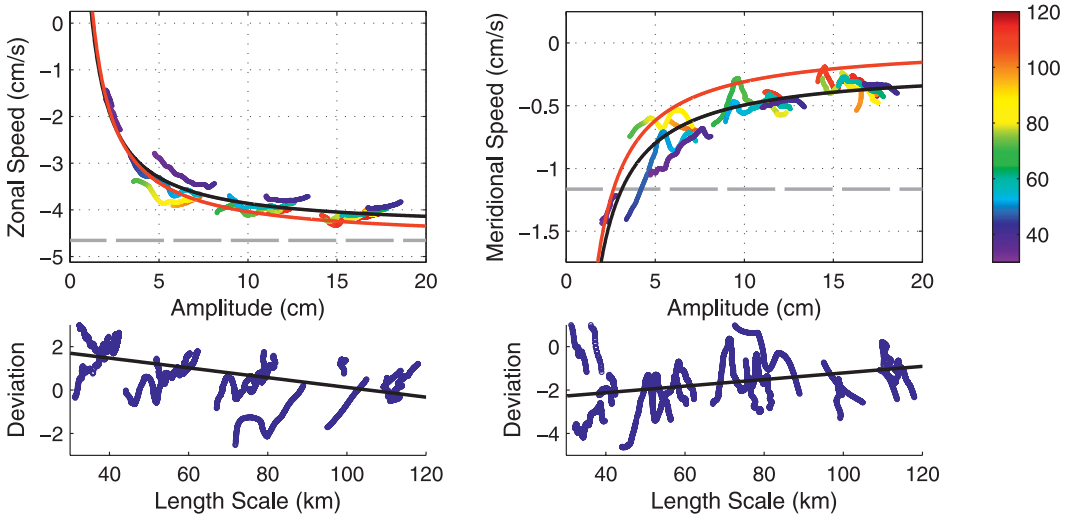

FIG. 9. (top) Eddy speed vs amplitude. The amplitude, speed, and length scale are plotted for each day of the eddy's evolution starting at day 200 until day 730 or until the eddy can no longer be tracked. In total, 5139 points are plotted. The black lines are the linear (inverse amplitude) best fit line to these points, $c_x(A) = 5.5A^{-1} - 4.4$ cm s^{-1} and $c_y(A) = -3.0A^{-1} - 0.19$ cm s^{-1}, whereas the red lines are from Eqs. (3) and (4). Points are colored with the eddy length scale (in km), suggesting a weak speed dependence on length scale. The dashed gray lines are the maximum group velocities of Rossby waves in the zonal and meridional directions. (bottom) The deviation of the eddy speed from the predicted relationship normalized by the variability, suggesting weak speed dependence on length scale. The results were filtered to only include isolated eddies in the quasi-stable state.

In the comoving frame, the height field (equivalent to the streamfunction or pressure field) becomes far more symmetric. The resulting largest instantaneous closed contour in the comoving frame is shown in red in Fig. 7; if the flow were steady in that frame, the fluid in this contour would be trapped and carried along with the eddy. For the region to truly trap fluid, the eddy's amplitude, length scale, shape, and translation speeds would all have to remain constant. Figure 8 shows that this is not the case.

The relative vorticity zero contour, where $\nabla^2\eta = 0$, shown in black in Fig. 7, remains nearly symmetric throughout the eddy lifetime, unlike the *e*-fold contour which was found to have far greater variability. For this reason it was found that the automated eddy tracking algorithm used in this monopole study was far more reliable when tracking the relative vorticity extremum and the contour of zero relative vorticity than tracking the sea surface height extremum and *e*-folding contour. Following Korotaev and Fedotov (1994), the inner core of an anticyclonic eddy is defined here as the region containing negative relative vorticity, whereas the outer ring is the surrounding region of positive relative vorticity.

For the initial Gaussian disturbance, the *e*-fold contour of sea surface height and contour of zero relative vorticity are identical, but, as can be seen in Fig. 7, this is not the case for the quasi-stable state. The height difference between the higher northwestern corner of the contour of zero relative vorticity and the lower southeastern corner require a net fluid transport to the southwest, which is responsible for the equatorward meridional deflection of this Northern Hemisphere anticyclonic eddy. Note that if we defined the eddy by contours of constant sea surface height there could be no net meridional transport across the eddy because the net transport is $\int_a^b \eta_x \, dx = \eta(b) - \eta(a)$, the difference of which is zero.

b. Meridional and zonal propagation speeds

The zonal speeds of the isolated eddies in the quasi-stable regime were found to be dependent on the eddy amplitude such that larger-amplitude eddies propagate significantly faster than smaller-amplitude eddies, as shown in Fig. 9. This is qualitatively consistent with the observed eddies, for which the eddies with largest ⅓ amplitudes propagate about 20% faster than the eddies with the ⅓ smallest amplitudes Chelton et al. (2011) (see Figs. 19 and 20 and the related discussion in section 4). Figure 9 also shows mild dependence on eddy length scale with smaller eddies propagating slightly more slowly. In general then, eddies larger in both amplitude and length scale propagate faster than eddies smaller in amplitude and length scale. The least squares fit to the inverse amplitude was found to be $c_x(A) = 5.3A^{-1} - 4.4$ cm s^{-1}. This is suggestive of a lower bound asymptote at -4.4 cm s^{-1}, which is close to the linear long-wave speed of 4.7 cm s^{-1}.

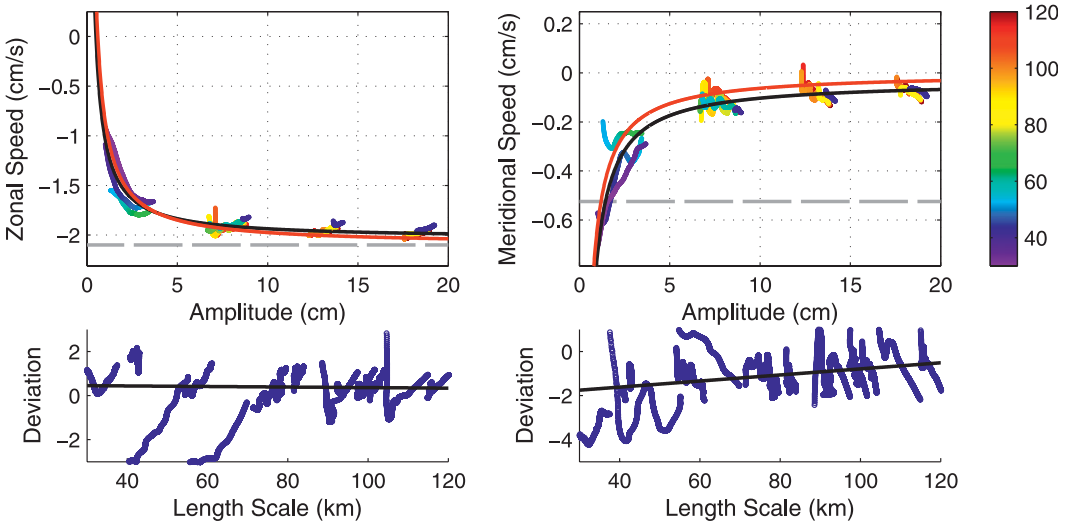

FIG. 10. Propagation speed of eddy vs eddy amplitude. As in Fig. 9, but at latitude 35°. The zonal and meridional inverse amplitude best fits lines are $c_x(A) = 1.0A^{-1} - 2.0$ cm s^{-1} and $c_y(A) = -0.71A^{-1} - 0.032$ cm s^{-1}, respectively.

That the zonal speed of the eddies is slower than the linear long-wave speed is consistent with previous experiments. The linear model considered in Flierl (1977) suggests that this should be the case at least for linearized Gaussians. In the case of the nonlinear model considered here, this is also consistent with the notion of "wave drag" caused by the excitation of Rossby waves forcing a slower propagation speed (Korotaev and Fedotov 1994).

The meridional speed of the eddy was similarly found to depend significantly on the amplitude of the eddy, as shown in Fig. 9; the meridional speed decreases with increasing amplitude. The least squares fit to the inverse amplitude was found to be $c_y(A) = -3.0A^{-1} - 0.19$ cm s^{-1}. Just as with the zonal propagation speed, there appears to be a weak dependence on the length scale of the eddy with meridional speed decreasing with increasing amplitude. However, unlike the zonal propagation speed, Fig. 9 shows the smaller-amplitude eddies exceed the maximum meridional Rossby wave group velocity. To obtain reliable meridional speeds, data points with amplitudes less than 2.0 cm were discarded because it was found that zonally propagating Rossby waves left over from the initialization and adjustment periods were interacting by catching up with the eddies (because their zonal propagation speed decreases as they evolve) and dramatically changing the meridional deflection.

Assuming that $c_x(A)$ asymptotes to the linear long-wave speed of 4.7 cm s^{-1} and then dividing the least squares fit regression coefficient (5.3) by this value reveals an amplitude scale of approximately 1.1 cm. This scale is suggestive of $N_{QG} = D(\beta_0 L_R^2)/(\sqrt{gD})$, the height scale that arises when all coefficients of Eq. (1) are forced to unity, which results in $N_{QG} = 1.3$ cm (in contrast to choosing a preferred scale such as $N_0 = 10$ cm as we have done). Given the observation that the linear long-wave speed of $\beta_0 L_R^2$ appears to be a lower bound asymptote, this suggests that the propagation speed c_x is dependent on the eddy amplitude A by

$$c_x(A) = \beta_0 L_R^2 \left(\frac{N_{QG}}{|A|} - 1 \right). \tag{3}$$

The corresponding meridional propagation would take the form

$$c_y(A) = -\frac{\beta_0 L_R^2}{2} \frac{N_{QG}}{A}. \tag{4}$$

These predicted dependencies are plotted in red in Fig. 9 and appear to most closely approximate the speed dependencies of the eddies with the longest length scales. To test the hypothesis that Eqs. (3) and (4) correctly describe the propagation speed dependency of quasigeostrophic eddies on eddy amplitude, the same experiment was run at latitude 35°, where the linear long-wave speed is 2.2 cm s^{-1} and $N_{QG} = 0.60$ cm. The results are shown in Fig. 10 and are consistent with the hypothesis.

The small-amplitude limits of Eqs. (3) and (4) result in seemingly nonsensical values. However, it is important to note that these results are for coherent, identified eddy features for which the length scale is also decreasing. The simultaneous decrease in amplitude and length scale keeps the eddies nonlinear by maintaining relatively large fluid velocities. Because the length scales are also small in this limit, it is not clear exactly what limiting speed should be expected.

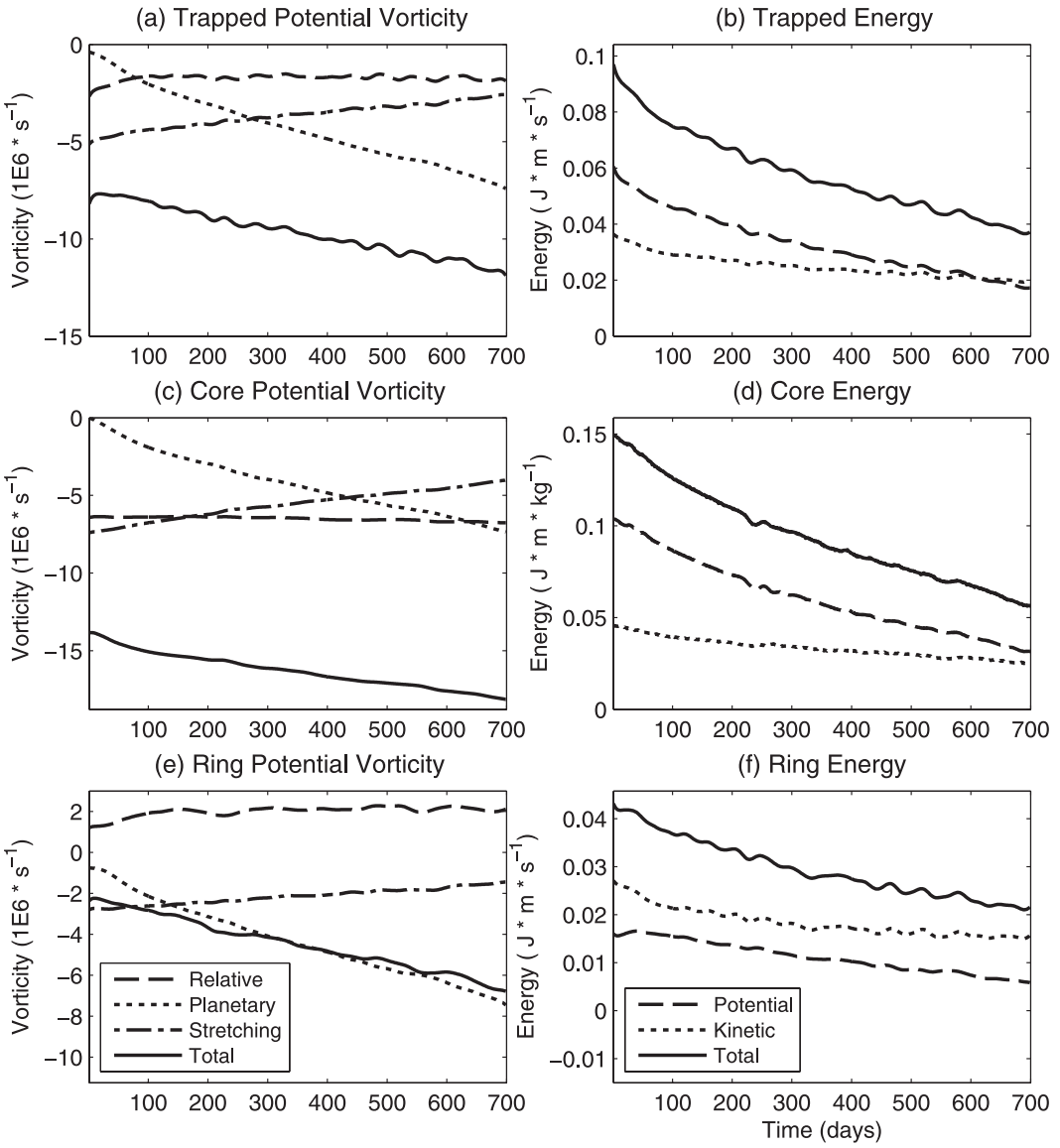

FIG. 11. Area-mean potential vorticity and energy within the entire trapped fluid region; the eddy core; and the eddy ring of an 80-km, 15-cm Gaussian initialized eddy. The trends are the same for the other quasi-stable eddies.

c. *Trapped fluid conservation properties*

If the fluid rotational speeds U in the eddy exceed its translation speed c, transforming coordinates into the comoving frame will result in closed streamlines within the eddy. The outermost closed streamline bounds the region where no fluid can escape, if the flow in the translating frame is steady. However, these quasi-stable eddies have slowly decaying amplitude and length scales (Fig. 8). The region of trapped fluid and the amplitude both decrease, meaning that the volume of trapped fluid actually decreases with time.

Conservation of potential vorticity for a fluid parcel has contributions from three terms, planetary vorticity, relative vorticity, and vortex stretching,

$$\frac{d}{dt}\left[\underbrace{\beta_0 y}_{\text{planetary vorticity}} + \underbrace{\frac{g}{f_0}\nabla^2\eta}_{\text{relative vorticity}} - \underbrace{\frac{f_0}{D}\eta}_{\text{vortex stretching}}\right] = 0. \tag{5}$$

Figure 11 shows the relative contributions from each of the three terms in potential vorticity conservation for

a Gaussian initialized eddy with 15-cm amplitude and 80-km length scale. In Fig. 11a, the values are found by integrating the terms over the entire instantaneous region of trapped fluid at each time and then dividing by its area. The trends for the planetary vorticity, vortex stretching, and total potential vorticity are the same for all other eddies that reach the quasi-stable state.

Even though the region of trapped fluid changes in time, it is clear how the planetary and vortex stretching terms should change for the average fluid parcel in the region. Because the eddy has a southward component of propagation on a β plane (y decreases), the contribution from planetary vorticity decreases in time (βy decreases). The decay of the eddy's amplitude (η decreases) causes an increase in contribution from vortex stretching ($-\eta$ increases). That the contribution from relative vorticity remains nearly constant throughout the eddy lifetime means that the eddy is maintaining a ratio between the negative relative vorticity from the eddy core and the positive relative vorticity in the outer ring (see Fig. 7, top right).

Energy can be divided into two terms, the kinetic energy

$$\frac{g^2}{f_0^2}(\eta_x^2 + \eta_y^2)$$

and the potential energy η^2. Figure 11b shows decreasing contributions of both kinetic and potential energy as the eddy evolves. The initial ratios of kinetic energy to potential energy depend on the initial conditions. For example, the 80-km, 15-cm eddy considered in Fig. 11b is initially dominated by potential energy, whereas a 40-km, 10-cm eddy is initially dominated by kinetic energy. Despite the partition differences for the two eddies, both display similar evolution characteristics, with the average energy per fluid parcel decreasing over time. This trend is similar to that described by Korotaev and Fedotov (1994) and Korotaev (1997), who suggest that this may be due to the radiation of energy by Rossby waves.

To investigate the advective properties of the eddies, both a passive tracer and floats were added to the model. The passive tracer $W(x, y, t)$ is a scalar field with no sources or sinks initialized with the value of its initial x position and then allowed to evolve with the equation

$$\frac{\partial W}{\partial t} + u\frac{\partial W}{\partial x} + v\frac{\partial W}{\partial y} = 0.$$

In addition to the passive tracer, floats were initialized with positions at each grid cell. The float positions are solved by estimating the velocity field at each time step using bilinear interpolation. The fates of the tracer field and floats over the lifetime of a westward-propagating monopole are investigated separately for the eddy core and the eddy ring in the following subsections.

1) EDDY CORE

We consider the eddy core first (recall that this is the region whose outer boundary is defined as the zero relative vorticity contour where $\nabla^2\eta = 0$). Fluid must be entrained, exactly trapped, lost, or some combination of entrainment and loss.

Can a new parcel of fluid be entrained in the eddy core? Recall that the eddy core for an anticyclonic eddy is a region of positive sea surface height and negative relative vorticity and consider what it would take for a fluid parcel with no height perturbation and no relative vorticity to enter the eddy core. To join the eddy core, the fluid parcel must increase its height and therefore decrease its vortex stretching contribution to the total potential vorticity. To balance this decrease in vortex stretching, the particle must come from 35 km north of the eddy for every 1 cm increase in height. In addition to the decrease in potential vorticity from vortex stretching, the particle must also decrease its relative vorticity from zero to become negative. If we consider the eddy at the instant shown in Fig. 7 where the contour of zero relative vorticity is at roughly 4 cm, this would mean that, for a parcel of fluid to even reach the boundary of the core, it must be displaced from its original rest location 140 km north of the eddy. However, the eddy's radial length scale is much less than 140 km and, because of the effect of the β gyre, the eddy is propagating southwestward. We must therefore conclude that a new fluid parcel will not be entrained in the eddy core. Exactly this effect can be seen in the x-tracer panel in Fig. 7 where on day 675 the eddy core still only contains fluid initially trapped within a region centered at $(x, y) = (0, 0)$ when the eddy was formed.

Do fluid parcels on the eddy core boundary remain on the boundary? For particles to remain on the $\nabla^2\eta = 0$ contour, the fluid flow must be tangential to the contour, and there can be no normal flow. To conserve potential vorticity [Eq. (5)], these particles must therefore obey

$$\beta_0\frac{dy}{dt} = \frac{f_0}{D}\frac{d\eta}{dt} \tag{6}$$

throughout their lifetimes. During the time it takes a parcel of fluid to circulate once around the core, the condition is quite reasonable to meet. As computed before, this only requires a particle to decrease its height by 1 cm for every 35 km of meridional displacement. Using Fig. 7, we can estimate the north–south extent of the zero contour of relative vorticity to be 100 km, and

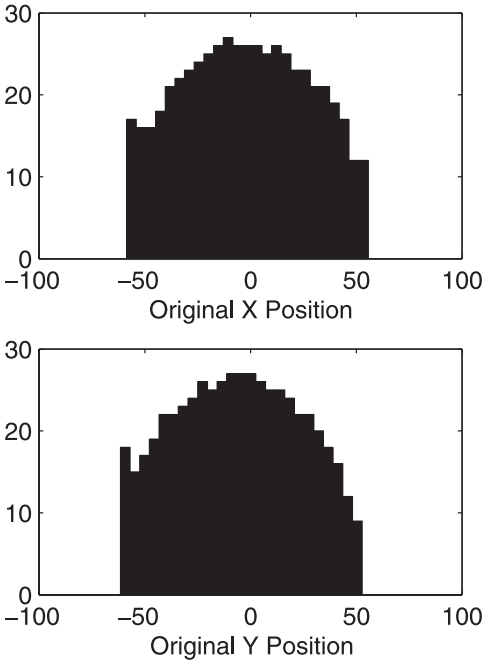

FIG. 12. Histograms of (top) the initial x position and (bottom) the initial y position of the fluid on day 675 in the core of an 80-km, 15-cm Gaussian initialized eddy. At this time, the eddy extremum is located at $x = -2247$ km and $y = -330$ km. Thus, the core contains only fluid from its starting point more than 2000 km away. An animation of the passive tracer field is included in the online supplemental material (available at the Journals Online Web site: http://dx.doi.org/10.1175/2011JPO4601.s1).

so our condition would require that the northern edge of the contour of zero relative vorticity be roughly 3 cm higher than the southern edge. Figure 7 shows that this is indeed the approximate difference. We can also use Eq. (6) with the parameters from this problem to compute a condition relating the meridional propagation to the amplitude decay, and we find that

$$9.0\,\frac{\mathrm{s}}{\mathrm{yr}}\cdot\frac{dy}{dt}=\frac{d\eta}{dt}. \tag{7}$$

This suggests that that meridional speed shown in Fig. 8 of approximately 0.5 cm s^{-1} must be offset by a height decay rate of approximately 4.5 cm yr^{-1} if a parcel is to remain on the zero contour. The observed height decay rate falls short of meeting this condition and instead has a decay rate closer to 3 cm yr^{-1}. Although these are estimates, the values computed for Fig. 8 are from the eddy maximum, and our condition in Eq. (7) is for the $\nabla^2\eta = 0$ contour, they are qualitatively correct. Such a particle therefore does not conserve potential vorticity and the assumption that particles remain on the contour of zero relative vorticity must be incorrect. To conserve potential vorticity [Eq. (5)] and account for this difference, this implies that particles must be increasing their relative vorticity and crossing the boundary of zero relative vorticity. The eddy core cannot entrain fluid and because the condition in Eq. (7) is not exactly met then it does not trap the fluid that defines its boundary, so the eddy core must be shedding fluid (equivalently, the boundary of the core is shrinking).

We can validate our entrainment conclusion with the model by considering the floats within the eddy core on day 675 and asking where they were on day zero. This can be seen in Fig. 12 where a histogram of the initial x and y positions of the fluid shows the fluid in the eddy core consists entirely of a subset of approximately the inner 50 km of the original fluid trapped in the core during the initialization of the 80-km eddy. The top panel of Fig. 13 shows these original float locations as red dots on top of the sea surface height for day 675, and the bottom panel shows the results of allowing a passive tracer to advect with the flow. The individual red dots are not discernible, because they are all clustered tightly within the core of the eddy at its initial center location of $(x, y) = (0, 0)$. The fluid was given a meridionally uniform color for each location in x on day zero according to the rainbow palette at the bottom of the figure.

Having established that no new fluid is entrained within the propagating eddy core defined by the contour of zero relative vorticity, we can more easily interpret Fig. 11c. Because the total potential vorticity becomes more negative on average, this implies that the eddy core is shedding fluid with higher potential vorticity.

Figure 14 shows the history of a float initially located in the eddy core, which remains in the eddy core for all 730 days of the model run. The oscillations in the individual contributions of the potential vorticity occur as the float circulates around the eddy core. The parcel of fluid tracked by the float finds that the total potential vorticity remained conserved, but the surface height adjusted to compensate for the loss of planetary vorticity from the equatorward displacement of the eddy, whereas the relative vorticity changed very little. The potential vorticity for the fluid parcel is within 0.1% of its initial value after 730 days. This is excellent confirmation that the numerical scheme is accurate because individual contributions to the potential vorticity vary by well over 50%.

2) EDDY RING

The eddy ring consists of fluid with positive relative vorticity, although with magnitude much smaller than the eddy core. The same possibilities for trapped fluid

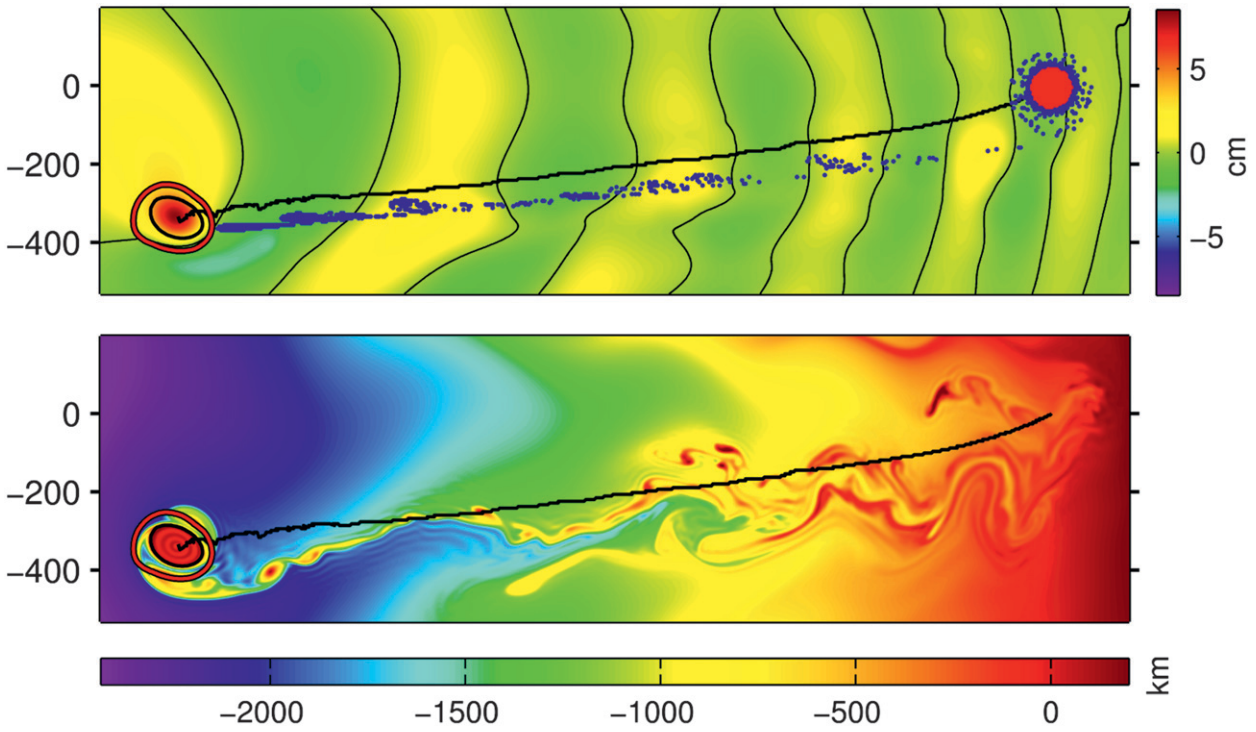

FIG. 13. Location of fluid advected on day 675. (top) SSH with the instantaneous trapped fluid contour (red) and relative vorticity zero contour (black). Blue circles show the day zero location of the floats in the eddy ring, whereas red circles show the location of floats in the eddy core. (bottom) A passive tracer equal to the initial (day 0) value of the zonal coordinate.

exist as with the core: fluid is either entrained, exactly trapped, lost, or some combination of entrainment and loss.

At the very least, the eddy ring will be collecting fluid shed from the shrinking boundary of the eddy core. In addition, however, the eddy ring will also entrain new surrounding fluid. An increase in height (and therefore a compensated increase in relative vorticity) is exactly what a fluid parcel requires to join the eddy ring. This can be seen from the histograms of the original locations of floats found in the ring on day 675, shown in Fig. 15, where it is clear that the eddy ring has collected (and also therefore released) fluid throughout its lifetime. These original float locations are shown in the top panel of Fig. 13 as blue dots on top of the sea surface height on day 675.

The average potential vorticity composition within the eddy ring over time for the 80-km, 15-cm eddy is shown in Fig. 11e. The contribution from planetary vorticity decreases and the vortex stretching contribution increases; again, both of these are obvious. The relative vorticity remains flat or mildly increases for all eddies. The average potential vorticity trend always decreases. This is because the ring is shedding fluid with higher potential vorticity and acquiring new fluid with lower potential vorticity, as we can see from the tracer in Fig. 13 and the histograms in Fig. 15.

Figure 16 shows the potential vorticity composition for a float that began in the eddy core, crossed to the eddy ring (all while circulating around the eddy center causing the oscillations) and was eventually ejected from the eddy. Notice that the potential vorticity for this float does not remain perfectly constant. Although most floats throughout the domain do conserve potential vorticity well, we find that floats crossing the relative vorticity zero contour often undergo rapid changes in potential vorticity while crossing the boundary. After examining a number of individual floats, we believe that this is an artifact of the strong gradients of u and v that are poorly resolved with bilinear interpolation, which also typically coincide with regions of strong potential vorticity gradients.

Although the linear model is generally associated with the assumption that fluid parcel advection is negligible, the Lagrangian motion implied by the geostrophic velocity field can still be computed ex post facto. The resulting motion is equivalent to the Stokes drift resulting from the interaction of two or more Rossby waves with the same frequency (not shown here). This can be seen in Fig. 17, which shows the same tracer fluid experiment seen in the bottom panel of Fig. 13 but using linear dynamics

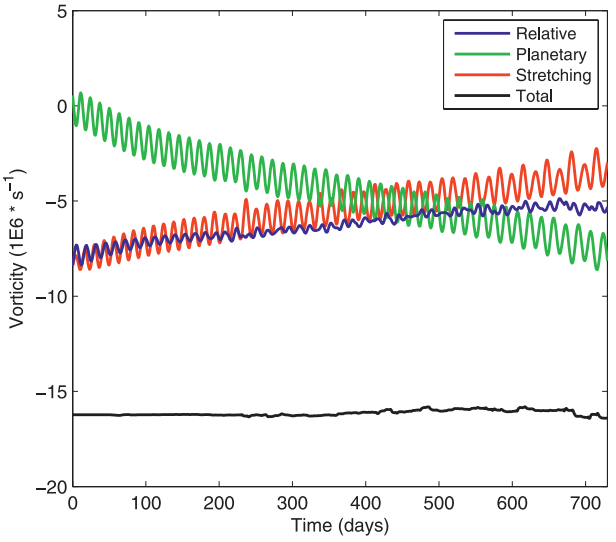

FIG. 14. Contributions to the total potential vorticity for a float initially at $x = 29$ km and $y = 26$ km. The float remains inside the core of the eddy for all 730 days. On day 730, the float was located at $x = -2400$ km and $y = -389$ km.

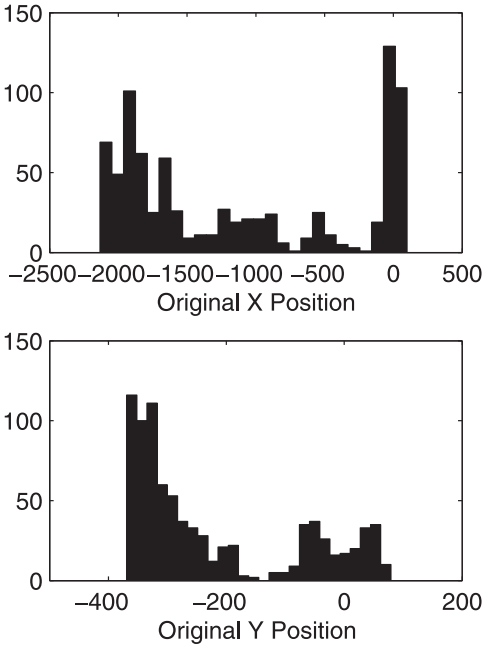

FIG. 15. As in Fig. 12, but histograms of (a) the initial x position and (b) the initial y position of the fluid in the ring on day 675. Thus, the ring contains a mixture of fluid from throughout its lifetime.

(when $\beta^{-1} = 0$). The resulting fluid transports are still valid provided that the advection of relative vorticity is small compared to the other terms in the potential vorticity Eq. (5), even if fluid parcels are advected at a finite distance. However, because the dynamics substantially change with the inclusion of the advection of relative vorticity, as seen in Fig. 1, we know that this condition is violated and the advection of relative vorticity is not negligible. Even with this inconsistent assumption, although fluid is transported over 1000 km, it still pales in comparison to the distance and efficiency with which fluid is transported by the coherent eddy in Fig. 13.

4. Discussion

Although it may seem surprising that the quasi-stable state of isolated nonlinear eddies identified here has not previously been identified, early numerical solutions of isolated quasigeostrophic eddies, such as McWilliams and Flierl (1979), have typically been restricted to times roughly as long the adjustment period identified here, likely because of computational resource limitations. The numerical study of Sutyrin et al. (1994) and Lam and Dritschel (2001) did consider times longer than the adjustment period but not significantly longer and for a smaller range of scales. Only by considering times after the adjustment period and discarding eddies that failed to reach the quasi-stable state do we find clear relationships between eddy amplitude and propagation speed, as in Fig. 9. The empirical Eqs. (3) and (4) appear to describe this relationship accurately; an analytical derivation of these equations would likely provide additional insight into the nature of the quasi-stable state.

Previous studies have attempted to formulate analytical estimates of the westward propagation speed of quasigeostrophic vortices by determining the speed of the center of mass (McWilliams and Flierl 1979; Cushman-Roisin et al. 1990). However, the center of mass is determined by integration over the entire domain (rather than a region localized around the eddy like the contour of zero relative vorticity used here) and does not appear to correlate with the speed of the tracked eddies. The approaches found in Korotaev (1997) and Nycander (2001) use the loss of energy through Rossby wave radiation to estimate the propagation speeds and may apply during the adjustment period but, based on comparisons to our numerical results, do not appear to apply to the quasi-stable state. The results of the analytical study Reznik et al. (2000) are only valid for time periods extending into the adjustment period where the eddy height decay rate is at its strongest and may explain why their results significantly underestimate the eddy's lifetime.

Although the isolated eddies in section 3 and the basin of eddies in section 2b are both governed by the same equation, Eq. (1), it is not necessarily true that the properties of one experiment applies to the other. First, is the shape of nonlinear zonal frequency–wavenumber

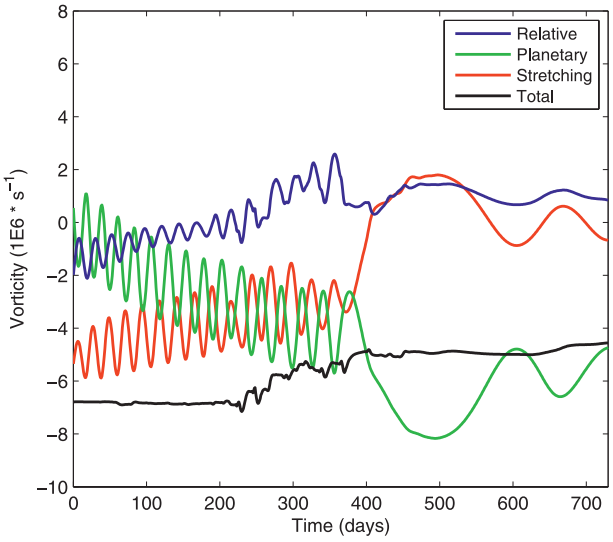

FIG. 16. Contributions to the total potential vorticity for a float initially at $x = 60$ km and $y = 26$ km. The float begins in the eddy core, crosses to the ring, and is eventually lost by the eddy. On day 730, the float was located at $x = -1113$ km and $y = -227$ km.

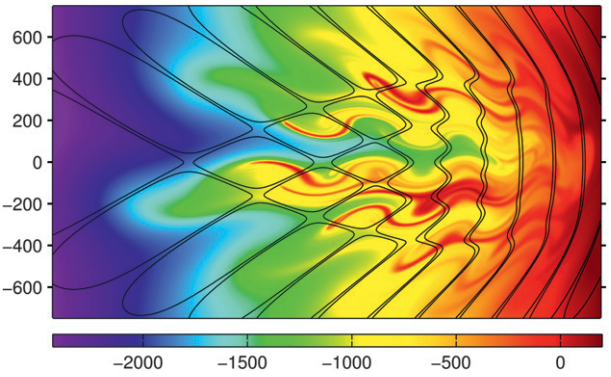

FIG. 17. Passive tracer on day 675 advected by an initially Gaussian disturbance evolved with linear dynamics. The contours of zero SSH are shown in black. As in Fig. 13 (bottom), but with linear dynamics.

spectra in Fig. 3 explained primarily by eddy–eddy interaction, or is it already represented in the monopole experiment? Second, does the eddy speed dependence on amplitude and length scale as shown in Fig. 9 also exist for the eddy seeding experiment?

In the first experiment, the zonal frequency–wavenumber spectra in Fig. 3 were repeated for isolated monopoles and are shown in Fig. 18. The spectra were averaged over multiple y slices to capture the power from the whole domain. The spectra of the isolated eddy and eddy basin evolved with linear dynamics appear nearly identical, and the spectra of the nonlinear experiments are also quite similar, but with two noticeable differences. First, the spectrum of the isolated eddy experiment shows a somewhat more distinct spur of power following the linear Rossby wave zonal dispersion relation than is found in the spectrum from the eddy seeding experiment. This is explained by the observation that the Rossby waves shed from the initial disturbance is still largely obeying linear dynamics in the monopole experiment, whereas in the seeding experiment there is relatively little free space between eddies (and therefore less room for features that obey linear dynamics). Second, the spectrum from the nonlinear eddy seeding experiment shows relatively less power at higher

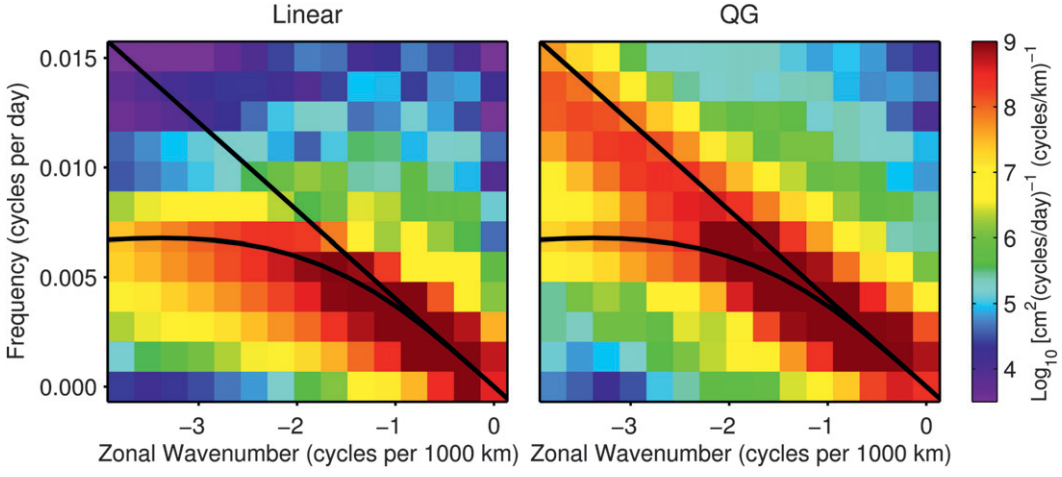

FIG. 18. Zonal frequency–wavenumber spectra for SSH of (left) the linear model and (right) the nonlinear model from the 730-day evolution of an initially Gaussian SSH of amplitude 15 cm and length scale 80 km. The black lines are the maximum (meridional wavenumber $l = 0$) Rossby wave zonal dispersion relation (curved) and its nondispersive limit (linear).

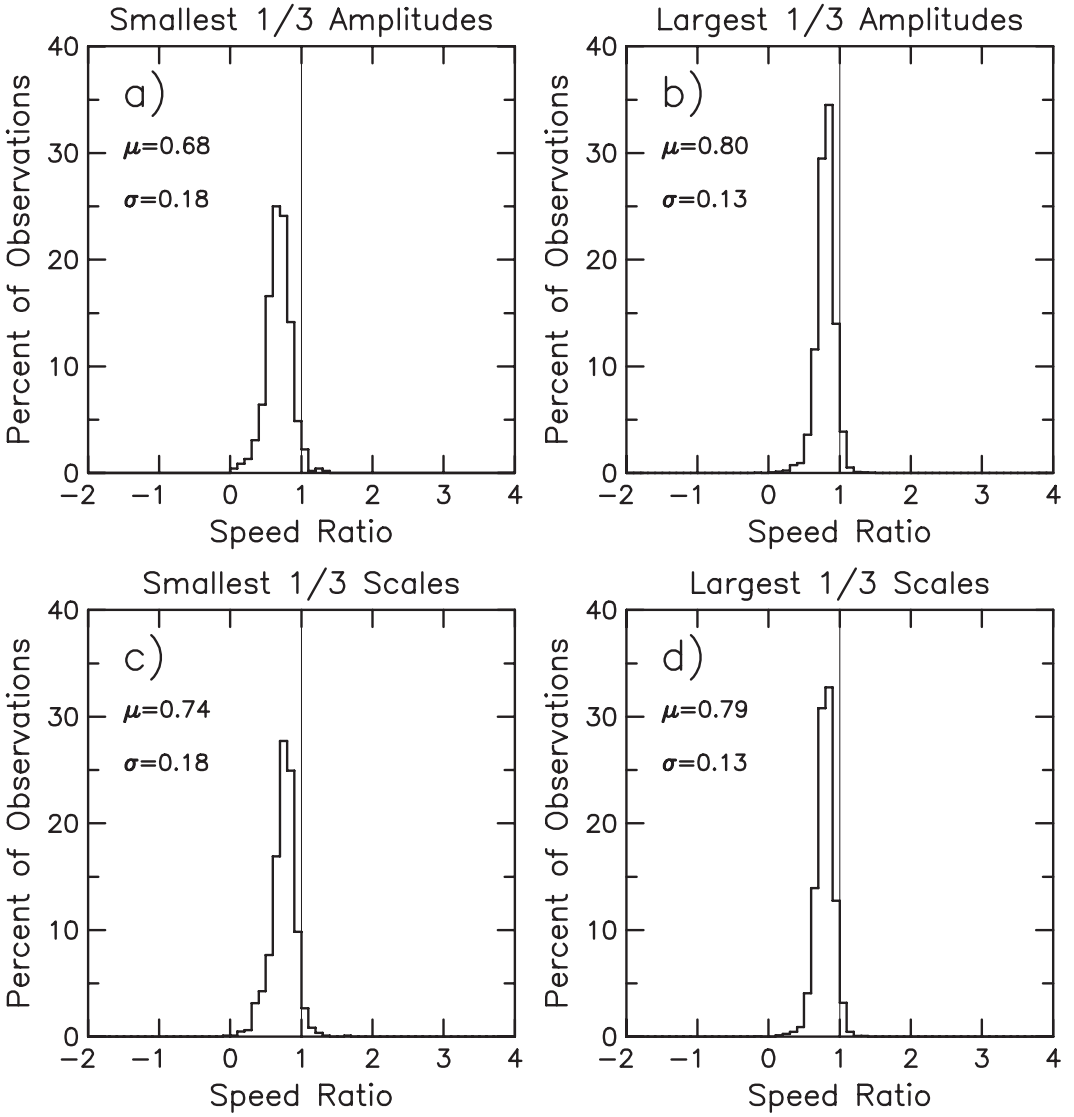

FIG. 19. Distributions of eddy speeds from the nonlinear model normalized by the nondisperisve Rossby wave phase speed separated into the eddies with (a) smallest 1/3 amplitudes; (b) largest 1/3 amplitudes; (c) smallest 1/3 length scales; and (d) largest 1/3 length scales.

wavenumbers than in the monopole experiment. This stronger shift in concentration of power from the larger wavenumbers to the smaller wavenumbers likely arises from the eddy–eddy interaction introduced in the eddy seeding experiment. This is consistent with the up-scale energy cascade of quasigeostrophic turbulence (Vallis 2006).

In the second experiment, it is shown that the eddy speed dependence on amplitude and length scale shown for isolated eddies in Fig. 9 also exists in the eddy seed experiment as well as for the altimeter observations (Chelton et al. 2011). Figure 19 shows the tracked eddies from the nonlinear eddy seeding experiment separated by amplitude and length scale. Just as for the isolated monopoles, propagation speed is strongly dependent on eddy amplitude and weakly dependent on eddy length scale. Figure 20 shows that this relationship also holds for the altimeter observations.

5. Conclusions

The long-term coherence of eddies observed and tracked by satellite altimetry more closely matches the evolution of isolated eddies in the nonlinear than in the linear model. Further, the spectral properties of the eddies observed by satellite altimetry are in excellent

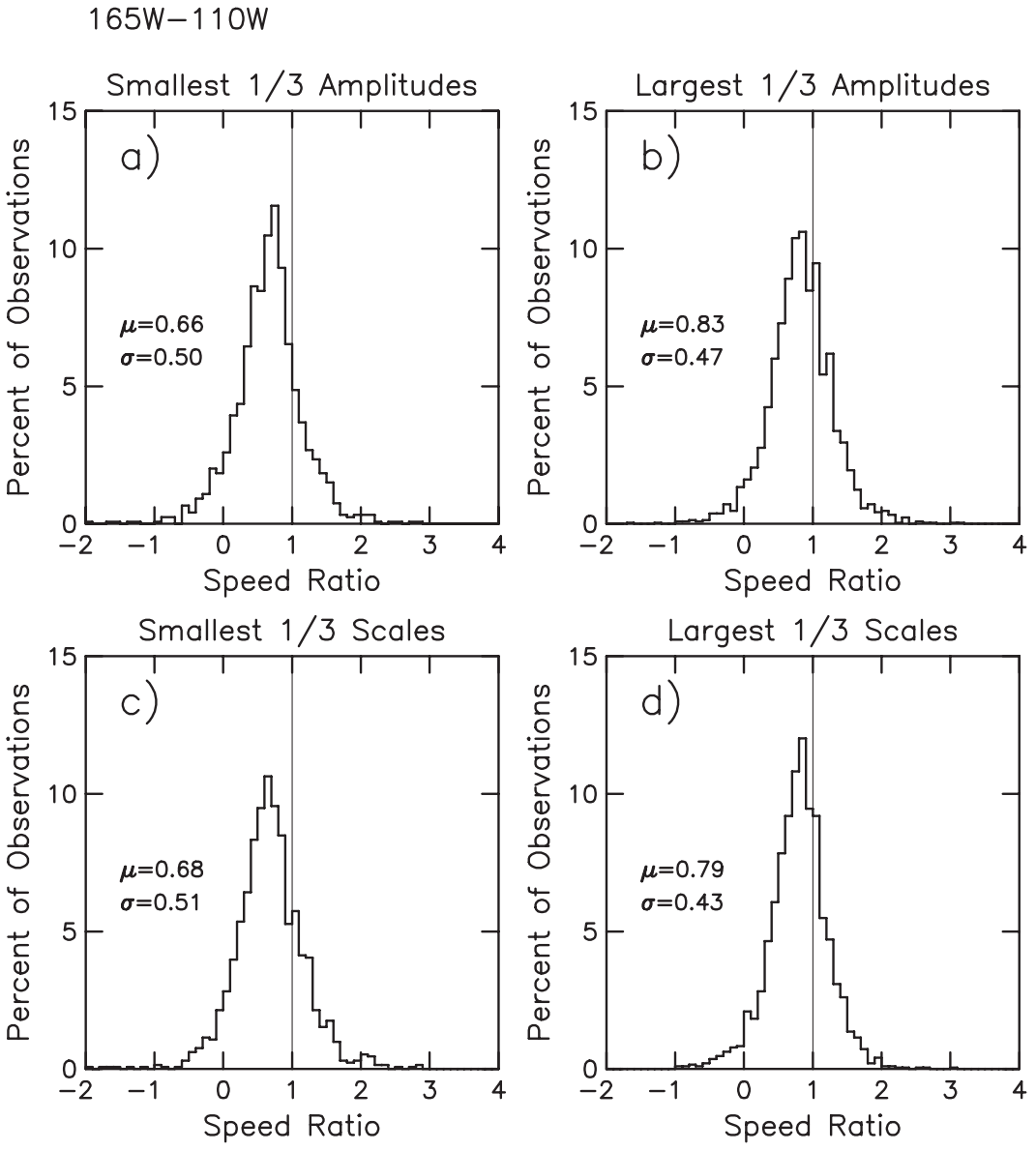

FIG. 20. As in Fig. 19, but for the altimeter observations of eddies in the eastern subtropical Pacific between 20° and 35°N and between 165° and 110°W.

agreement with the spectrum from the basin-scale eddy seeding experiment for the nonlinear quasigeostrophic model. Taken together, we find this to be convincing evidence that the signals observed in the high-resolution satellite observations (Chelton et al. 2007, 2011) represent eddies obeying nonlinear dynamics.

In an effort to understand the characteristics of quasigeostrophic eddies, we conducted a study of the long-term evolution of isolated eddies. Gaussian initialized eddies have three distinct regimes in their evolution, of which only two have previously been characterized. What was once believed to be a quasi-stable state turns out to be better characterized as an adjustment period, and only at lifetimes of approximately $15(\beta_0 L_R)^{-1}$ does a truly quasi-stable state emerge.

The quasi-stable state is characterized by zonal and meridional propagation speeds strongly dependent on the inverse amplitude of the eddy, with larger amplitudes tending toward the long-wave limit of linear Rossby waves. All propagation speeds for the monopole experiments are slower than this limit, and this is thought to be an effect of the wave drag caused by the excitation of Rossby waves. This same speed dependence was found in the eddy seeding experiment as well as the enhanced eddy resolving

observations (Chelton et al. 2007, 2011), which found zonal propagation speeds to be strongly dependent on amplitude and weakly dependent on length scale. However, the nonlinear model has a smaller variability in the distribution of eddy speeds compared with the observations, and we believe that this is a limitation of quasigeostrophic theory or the neglect of the effects of variations in the background mean flow on the potential vorticity gradient.

The quasigeostrophic eddies were shown to transport a substantial amount of fluid over long distances. At any point during an eddy's lifetime, 100% of the fluid in the core is from the initialization location, where the core is defined as the region interior to the zero contour of the relative vorticity. This is in contrast to the instantaneously defined trapped fluid region, determined by transforming into coordinates comoving with the eddy, which does not well describe the boundary of the retained fluid. In this sense, the core of the eddy is a ''perfect'' transporter of fluid and carries the same parcels of fluid for thousands of kilometers during its slow decay. The ring of fluid with opposite signed relative vorticity fluid around the eddy is approximately bounded by the zero contour of relative vorticity and the region of trapped fluid but transports fluid in a very different manner. The ring entrains and sheds fluid throughout its lifetime, moving some parcels of fluid hundreds of kilometers and others thousands of kilometers.

In light of our conclusion that the satellite observations are not Rossby waves, these transport properties have significant implications. Linear Rossby waves cannot transport fluid nearly as effectively, and therefore most energy transferred is in the form of kinetic and potential energy. The nonlinear eddies, in contrast, are capable of transporting relatively large quantities of fluid and therefore can carry energy in the form of heat, in addition to the kinetic and potential energy carried by wave fluctuations, as well as other material properties and dissolved materials that may have biological importance.

A number of issues regarding the individual properties of quasigeostrophic eddies still need to be resolved. Although an empirical relationship between the propagation speed and the eddy amplitude was found, a satisfactory analytical theory for this relationship has not yet been developed. Further, we believe that the ideas of radiative Rossby wave energy loss should be applicable outside the adjustment period explored in Korotaev (1997) and Nycander (2001). Analytical formulations for the relationships between eddy amplitude decay rates and propagation speed may be possible.

Acknowledgments. Much thanks to Michael G. Schlax for eddy tracking in the seeding experiments and for compiling the associated figures. This research was supported by the National Science Foundation, Award 0621134, and by the National Aeronautics and Space Administration, Grant NNX08AR37G.

REFERENCES

Anderson, D., and A. Gill, 1975: Spin-up of a stratified ocean, with applications to upwelling. *Deep-Sea Res.,* **22,** 583–596.

Canuto, C., 2006: *Spectral Methods: Fundamentals in Single Domains*. Springer, 563 pp.

Chelton, D. B., and M. Schlax, 1996: Global observations of oceanic Rossby waves. *Science,* **272,** 234–238.

——, R. A. deSzoeke, M. G. Schlax, K. E. Naggar, and N. Siwertz, 1998: Geographical variability of the first baroclinic Rossby radius of deformation. *J. Phys. Oceanogr.,* **28,** 433–460.

——, M. G. Schlax, R. M. Samelson, and R. A. de Szoeke, 2007: Global observations of large oceanic eddies. *Geophys. Res. Lett.,* **34,** L15606, doi:10.1029/2007GL030812.

——, ——, and ——, 2011: Global observations of nonlinear mesoscale eddies. *Prog. Oceanogr.,* doi:10.1016/j.pocean.2011.01.002, in press.

Cushman-Roisin, B., B. Tang, and E. Chassignet, 1990: Westward motion of mesoscale eddies. *J. Phys. Oceanogr.,* **20,** 758–768.

Durran, D., 1991: The third-order Adams–Bashforth method: An attractive alternative to leapfrog time differencing. *Mon. Wea. Rev.,* **119,** 702–720.

Fiorino, M., and R. Elsberry, 1989: Some aspects of vortex structure related to tropical cyclone motion. *J. Atmos. Sci.,* **46,** 975–990.

Flierl, G., 1977: The application of linear quasigeostrophic dynamics to Gulf Stream rings. *J. Phys. Oceanogr.,* **7,** 365–379.

——, 1984: Rossby wave radiation from a strongly nonlinear warm eddy. *J. Phys. Oceanogr.,* **14,** 47–58.

——, V. Larichev, J. McWilliams, and G. Reznik, 1980: The dynamics of baroclinic and barotropic solitary eddies. *Dyn. Atmos. Oceans,* **5,** 1–41.

Fu, L., and D. Chelton, 2001: Large-scale ocean circulation. *Satellite Altimetry and the Earth Sciences: A Handbook of Techniques and Applications,* L. Fu and A. Cazenave, Eds., International Geophysics Series, Vol. 69, Academic Press, 133–169.

Gelb, A., and J. Gleeson, 2001: Spectral viscosity for shallow water equations in spherical geometry. *Mon. Wea. Rev.,* **129,** 2346–2360.

Karamanos, G., and G. Karniadakis, 2000: A spectral vanishing viscosity method for large-eddy simulations. *J. Comput. Phys.,* **163,** 22–50.

Killworth, P., and J. Blundell, 2005: The dispersion relation for planetary waves in the presence of mean flow and topography. Part II: Two-dimensional examples and global results. *J. Phys. Oceanogr.,* **35,** 2110–2133.

——, D. Chelton, and R. de Szoeke, 1997: The speed of observed and theoretical long extratropical planetary waves. *J. Phys. Oceanogr.,* **27,** 1946–1966.

Korotaev, G., 1997: Radiating vortices in geophysical fluid dynamics. *Surv. Geophys.,* **18,** 567–619.

——, and A. Fedotov, 1994: Dynamics of an isolated barotropic vortex on a beta-plane. *J. Fluid Mech.,* **264,** 277–301.

Lam, J. S.-L., and D. Dritschel, 2001: On the beta-drift of an initially circular vortex patch. *J. Fluid Mech.,* **436,** 107–129.

Maltrud, M., and G. Vallis, 1993: Energy and enstrophy transfer in numerical simulations of two-dimensional turbulence. *Phys. Fluids,* **5A,** 1760–1775.

McWilliams, J., and G. Flierl, 1979: On the evolution of isolated, nonlinear vortices. *J. Phys. Oceanogr.,* **9,** 1155–1182.

Morrow, R., F. Birol, D. Griffin, and J. Sudre, 2004: Divergent pathways of cyclonic and anti-cyclonic ocean eddies. *Geophys. Res. Lett.,* **31,** L24311, doi:10.1029/2004GL020974.

Nycander, J., 2001: Drift velocity of radiating quasigeostrophic vortices. *J. Phys. Oceanogr.,* **31,** 2178–2185.

Pasquetti, R., 2005: High-order LES modeling of turbulent incompressible flow. *C. R. Mec.,* **333,** 39–49.

Pedlosky, J., 1987: *Geophysical Fluid Dynamics*. 2nd ed. Spring-Verlag, 710 pp.

Reznik, G., and W. Dewar, 1994: An analytical theory of distributed axisymmetric barotropic vortices on the β-plane. *J. Fluid Mech.,* **269,** 301–301.

——, R. Grimshaw, and E. Benilov, 2000: On the long-term evolution of an intense localized divergent vortex on the beta-plane. *J. Fluid Mech.,* **422,** 249–280.

Samelson, R. M., 2010: An effective-β vector for linear planetary waves on a weak mean flow. *Ocean Modell.,* **32** (3–4), 170–174.

Sutyrin, G., and G. Flierl, 1994: Intense vortex motion on the beta plane: Development of the beta gyres. *J. Atmos. Sci.,* **51,** 773–790.

——, J. Hesthaven, J. Lynov, and J. Rasmussen, 1994: Dynamical properties of vortical structures on the beta-plane. *J. Fluid Mech.,* **268,** 103–131.

Tadmor, E., 1989: Convergence of spectral methods for nonlinear conservation laws. *SIAM J. Numer. Anal.,* **26,** 30–44.

Tailleux, R., and J. McWilliams, 2001: The effect of bottom pressure decoupling on the speed of extratropical, baroclinic Rossby waves. *J. Phys. Oceanogr.,* **31,** 1461–1476.

Vallis, G., 2006: *Atmospheric and Oceanic Fluid Dynamics: Fundamentals and Large-Scale Circulation*. Cambridge University Press, 745 pp.